ChemComm

COMMUNICATION

View Article Online
View Journal | View Issue

Cite this: *Chem. Commun.*, 2025, **61**, 2087

Received 10th September 2024,
Accepted 30th December 2024

DOI: 10.1039/d4cc04659e

rsc.li/chemcomm

Cr-MOF composited with facet-engineered bimetallic alloys for inducing photocatalytic conversion of CO_2 to C_2H_4†

Xiang-Yu Lu, Peng Wang,* Zhao-Feng Qiu and Wei-Yin Sun *

The design of efficient photocatalysts is crucial for photocatalytic CO_2 reduction. This study developed photocatalysts based on MIL-101(Cr) composited with a facet-engineered Pt/Pd nanoalloy (PPNA). Photocatalytic performance evaluations show that MIL-101(Cr) loaded with PPNA exposing {111} facets, namely M-A(111), exhibits a CO_2 to C_2H_4 conversion rate of 9.5 μmol g^{-1} h^{-1} in addition to the CO and CH_4, whereas M-A(100) with PPNA exposing {100} facets gives CO_2 conversion rates of 33.2 for CO and 9.3 μmol g^{-1} h^{-1} for CH_4 without C_2H_4. *In situ* FT-IR revealed that M-A(111) can readily form C_2 intermediates during the reaction. This work offers a strategy for the design of photocatalysts for CO_2 reduction to C_2H_4.

Photocatalytic conversion of carbon dioxide (CO_2) into valuable fuels as well as chemicals like carbon monoxide (CO), methane (CH_4) and ethylene (C_2H_4) has emerged as one of the most promising methods for effectively reducing CO_2 concentration.[1,2] Among these products, C_2H_4 is particularly interesting because of its importance in the chemical industry as a basic raw material. However, challenges such as the high energy barriers for activating CO_2 followed by C–C coupling and the low rates of multi-electron transfer restrict the CO_2 reduction reaction (CO_2RR), resulting primarily in C_1 products such as CO and CH_4.[3,4] Although strategies involving the introduction of single atoms,[5,6] metal alloys[7,8] and Cu species[9,10] have been employed to enhance the efficiency of CO_2 conversion to C_2H_4, the designed photocatalysts are still limited and fall short in improving photocatalytic activity and product selectivity.

Single metal photocatalysts rarely exhibit both good C–C coupling performance and appropriate desorption ability for C_2H_4* intermediates simultaneously.[11] Typically, metals such as Ag and Pt facilitate desorption,[12,13] while Pd and Cu promote C–C coupling.[14,15] However, with appropriate design, bimetallic species can endow the catalyst with both capabilities of C–C coupling and intermediate desorption.[16] Recently, there have been studies exploring the application of binary metal catalysts for CO_2 photoreduction;[17] however, the efficiency in producing multicarbon (C_{2+}) products remains unsatisfactory and further investigations are required.

In recent years, facet engineering of metal–organic frameworks (MOFs) has been demonstrated to be an effective way of tuning the performance of photocatalytic CO_2 reduction.[18,19] In addition, facet engineered MOF-metal nanoparticle composites show improved CO_2RR.[20] In this study, facet engineered bimetallic nanoalloys rather than MOFs, namely Pt/Pd nanoalloys (PPNAs), were employed to composite with a classic Cr-MOF, MIL-101(Cr) for the creation of novel photocatalysts. Notably, by simply altering the reaction conditions, the exposed crystal facets of PPNA can be easily tuned, thereby controlling the types of alloy facets post-loading. The combination of MIL-101(Cr) with PPNA nanoparticles exposing {111} facets offers sample M-A(111) and enables photocatalytic CO_2 reduction to C_2H_4 under simulated sunlight; in contrast, no C_2H_4 was achieved for the sample M-A(100) with PPNA exposing {100} facets. Experimental results demonstrate that the synergistic interactions between the MIL-101(Cr) and {111} facets of the alloy generate highly stable reaction intermediates, further facilitating efficient C–C bond formation.

The synthetic procedure for the M-A(111) and M-A(100) samples is illustrated in Scheme 1 and the details for the preparation are given in the ESI.† Notably, PPNA particles exposing {111} facets were achieved by using K_2PtCl_4 and Na_2PdCl_4 with the presence of polyvinylpyrrolidone (PVP, MW = 24 000) and formaldehyde solution (40%) at pH = 4, and heating at 180 °C for 2 h. Following the same procedure using KBr and KI instead of formaldehyde at pH = 3 under heating at 160 °C for 4 h, PPNA particles exposing {100} facets were isolated.

MIL-101(Cr) has been recognized as an outstanding photocatalyst with the capability to catalyze the conversion of CO_2 into various products.[21] To further explore its potential, we synthesized MIL-101(Cr) powder ensured by scanning electron microscopy (SEM) (Fig. S1a, ESI†). Subsequently, we precisely

Coordination Chemistry Institute, State Key Laboratory of Coordination Chemistry, School of Chemistry and Chemical Engineering, Nanjing National Laboratory of Microstructures, Collaborative Innovation Center of Advanced Microstructures, Nanjing University, Nanjing 210023, China. E-mail: pengw907@nju.edu.cn, sunwy@nju.edu.cn

† Electronic supplementary information (ESI) available. See DOI: https://doi.org/10.1039/d4cc04659e

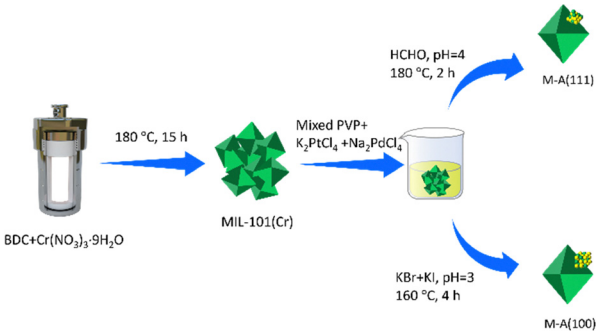

Scheme 1 Synthesis of M-A(111) and M-A(100).

reduced $PtCl_4^{2-}$ and $PdCl_4^{2-}$ adsorbed on MIL-101(Cr) to form a catalyst composed of MIL-101(Cr) and PPNA exposing the {111} facets, which is designated as M-A(111) (Fig. S1b, ESI†). To gain a clear understanding of its morphology, we examined the catalyst using transmission electron microscopy (TEM). The TEM images revealed uniformly dispersed nanoparticles on the surface of MIL-101(Cr) with no significant agglomeration (Fig. 1a). High-resolution TEM (HRTEM) images further confirm the presence of the loaded PPNA (Fig. 1b). The nanoparticles exhibit distinct lattice patterns and fast Fourier transform (FFT) images (Fig. S2 and S4a ESI†), with a lattice spacing of 0.225 nm corresponding to the {111} facets of PPNA (Fig. S4b, ESI†). We further employed high-angle annular dark-field scanning transmission electron microscopy-energy dispersive X-ray spectroscopy (HAADF-STEM-EDS) for line scan analysis of individual Pt/Pd elements and elemental mapping of the entire sample. No significant segregation of Pt and Pd was observed within the sample (Fig. 1c–e), indicating a quasi-uniform distribution of Pt/Pd elements throughout the particles and the formation of a nanocrystalline alloy structure. Additionally, we performed powder X-ray diffraction (PXRD) analysis for the sample. The results show that the diffraction pattern of the prepared composite material closely matched with that of MIL-101(Cr), with the exception of metallic peaks appearing at 39.8° and 46.3°, indicating the retention of the MIL-101(Cr) structure after PPNA loading (Fig. S5, ESI†).

Importantly, the morphology and facet of the PPNA particles can be controlled by adjusting the reduction environment and conditions for reducing $PtCl_4^{2-}$ and $PdCl_4^{2-}$.[22] We conducted experiments aimed at synthesizing PPNA with fully exposed {100} crystal facets. By introducing small amounts of Br^- and I^- into the reaction system and adjusting the pH, we successfully obtained PPNA with exposed {100} facets (see Experimental section, ESI†). As shown in Fig. S4d, ESI,† the lattice spacing of 0.194 nm corresponds to the {100} facets of PPNA, further corroborated by the associated FFT image (Fig. S3 and S4c, ESI†). Consequently, using the same preparation method, we designed another MIL-101(Cr) composite catalyst loaded with PPNA exposing the {100} facets, named M-A(100) (Fig. S1c, ESI†). As illustrated in Fig. 2a, TEM analysis revealed a similar structure to that of M-A(111) with uniformly dispersed PPNA particles. However, HRTEM observations show that the loaded PPNA exhibits a cubic morphology (Fig. 2b), with the exposed facets varying from {111} to {100}. The results of HAADF-STEM, elemental mapping and HAADF-STEM-EDS ensure the quasi-uniform distribution of Pt/Pd elements in M-A(100) (Fig. 2c–e), similar to that in M-A(111) (Fig. 1c–e). PXRD diffraction patterns also display corresponding metallic peaks, but with increased intensity (Fig. S5, ESI†), suggesting better crystallinity for the PPNA with exposed {100} facets. We further investigated the formation of distinct crystal facets by varying the reaction temperature, reducing agent, *etc.* (Fig. S6–S8, ESI†) and the possible atomic stacking modes of the two PPNAs are presented in Fig. S9 (ESI†). FT-IR and X-ray photoelectron spectroscopy (XPS) confirm that the structures of all samples are well preserved and maintained intact throughout the preparation process (Fig. S10, ESI†). Inductively coupled plasma mass spectrometry (ICP-MS) measurements determined that the Pt and Pd contents in both M-A(111) and M-A(100) catalysts are 1.8 wt% and 0.9 wt%, respectively. High-resolution XPS was employed to analyze the surface states of the Pt and Pd elements in both catalysts. Compared to M-A(111), the Pd 3d XPS peak of M-A(100) slightly shifts to high binding energy, while the Pt 4f XPS peak slightly shifts towards low binding energy (Fig. S11, ESI†). This implies that the two PPNAs possess different electronic distributions, which will likely lead to distinct behavior in the CO_2RR. Furthermore, Cr 2p XPS spectra show that, compared to MIL-101(Cr), the Cr binding energy in the PPNA-loaded catalyst decreases (Fig. S12a, ESI†), indicating an increase in its electron density. This suggests the occurrence of electron transfer between PPNA and MIL-101(Cr).

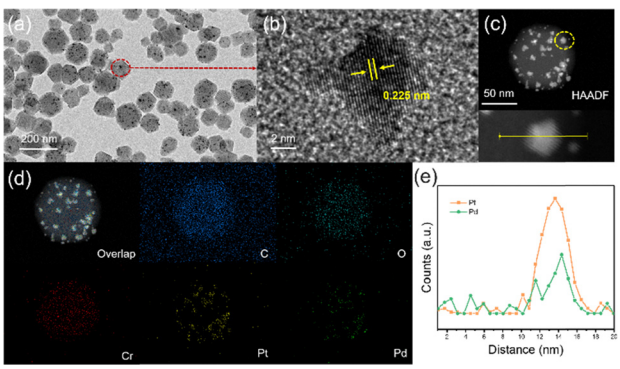

Fig. 1 For M-A(111): (a) TEM image; (b) HRTEM; (c) HAADF-STEM image; (d) elemental mapping. (e) HAADF-STEM-EDS line scan profile of a single PPNA, highlighted by the yellow line in Fig. 1c.

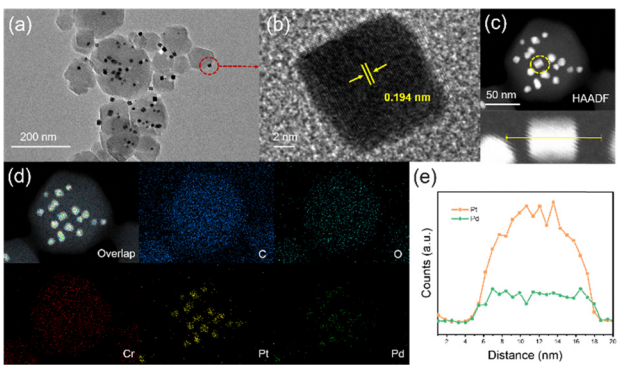

Fig. 2 For M-A(100): (a) TEM image; (b) HRTEM; (c) HAADF-STEM image; (d) elemental mapping. (e) HAADF-STEM-EDS line scan profile of a single PPNA, highlighted by the yellow line in Fig. 2c.

Photocatalytic CO_2RR tests were conducted for the varied catalysts. Firstly, it is noticeable that the rates of the CO_2 reduction products of M-A(111) and M-A(100) are significantly higher than those of pure MIL-101(Cr) (Fig. 3a), indicating that the incorporation of PPNA markedly enhanced the CO_2RR performance. Secondly, M-A(111) not only exhibits a high CH_4 conversion rate but also achieves a C_2H_4 conversion rate of 9.5 μmol g^{-1} h^{-1}. In contrast, M-A(100) and MIL-101(Cr) demonstrate no capability for conversion of CO_2 into C_2H_4, as confirmed by gas chromatography data (Fig. S13, ESI†). Notably, a physical mixture of PPNA and MIL-101(Cr) exhibits no significant improvement in performance compared to pure MIL-101(Cr) (Fig. S12b, ESI†), confirming the presence of interactions between PPNA and MIL-101(Cr) in the M-A(111)/(100) system. The results not only show that the composition of MOF with metal nanoparticles can improve the CO_2RR performance,[23–25] but also demonstrate the impact of the crystal facet on the CO_2RR.[26–28] In addition, under the identical conditions, a series of control experiments were performed for M-A(111). No products of CO, CH_4, or C_2H_4 were detected in the absence of CO_2 (in Ar), photocatalyst or light (Fig. 3b). Furthermore, experiments using labeled $^{13}CO_2$ support the same results, with gas chromatography-mass spectrometry (GC-MS) detecting signals corresponding to $^{13}C_2H_4$, ^{13}CO and $^{13}CH_4$ at m/z = 30, 29 and 17, respectively (Fig. 3c). This confirms that the carbon sources of the observed products originate from the initial CO_2 input rather than from other sources. Besides, the photostability was evaluated. As shown in Fig. 3d, M-A(111) maintains its catalytic activity after three uninterrupted cycles. TEM data and PXRD patterns in Fig. S14 (ESI†) indicate that the structure of the catalyst remained after the photocatalytic reaction.

A series of photochemical and electrochemical tests were conducted for the catalysts, revealing the underlying factors contributing to the superior photocatalytic performance. UV-visible diffuse reflectance data indicate that all catalysts exhibit broad light absorption capabilities (Fig. S15a, ESI†). The band gap widths are 2.78, 2.72 and 2.71 eV for MIL-101(Cr), M-A(111) and M-A(100), respectively, determined through Tauc analysis (Fig. S15b, ESI†). The valence band (VB) positions at 1.72, 1.53 and 1.95 eV for MIL-101(Cr), M-A(111) and M-A(100), respectively, were identified by using XPS valence band spectra, as shown in Fig. S15c, ESI.† The band gap diagram (Fig. S15d, ESI†) clearly shows that the LUMO levels of all catalysts are lower than the reduction potentials required for the conversion of CO_2 to CO, CH_4 and C_2H_4, suggesting that they have capacity for CO_2 reduction. To investigate the charge transfer processes within the catalysts, photoluminescence spectra and time-resolved fluorescence spectroscopy were utilized. The fluorescence quenching in M-A(111) was the most significant, indicating high carrier separation efficiency (Fig. S16a, ESI†). Besides, time-resolved fluorescence spectra show an average lifetime of 2.64 ns for M-A(111), shorter than the ones of MIL-101(Cr) (2.84 ns) and M-A(100) (2.73 ns) (Fig. S16b–d, ESI†), suggesting a rapid decay rate. The results indicate that M-A(111) has a faster charge transfer rate from ligand to PPNA than MIL-101(Cr) and M-A(100). Photoelectrochemical measurements and electrochemical impedance spectroscopy (EIS) were performed to assess the separation efficiency of the photoexcited charge carriers and the resistance levels of the catalysts under visible light irradiation. As shown in Fig. S17a and b, ESI,† M-A(111) exhibits the highest transient photocurrent response and the lowest resistance compared to other samples, indicating a high interfacial charge transfer rate (Scheme S1, ESI†).

To further monitor the photocatalytic CO_2 reduction process, *in situ* FT-IR spectroscopy was employed and the results are illustrated in Fig. 4. Upon light irradiation, the band at 1018 cm^{-1} is attributed to bicarbonate (HCO_3^-),[29] the one at 1320 cm^{-1} corresponds to monodentate carbonate (m-CO_3^{2-}),[30] and the one at 1743 cm^{-1} is assigned to the chelating bidentate carbonate (c-CO_3^{2-}).[31] The bands at 1108 and 1374 cm^{-1} are associated with CH* and CH_2*, respectively,[29] while the ones at 1253 and 1620 cm^{-1}

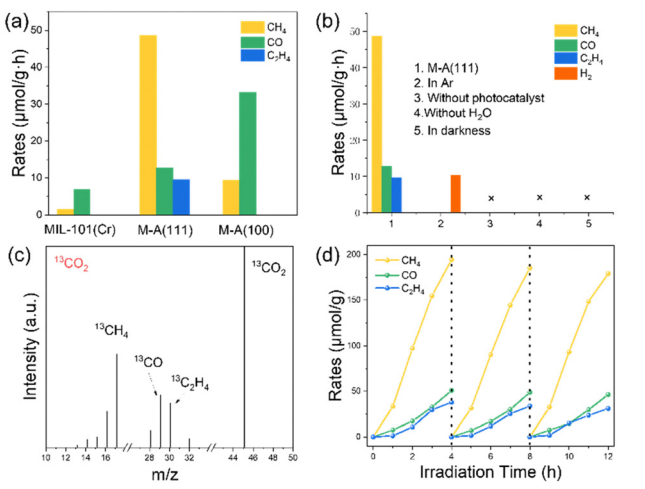

Fig. 3 (a) Product formation rates for varied catalysts and (b) photocatalytic CO_2 reduction results under varied reaction conditions. (c) GC-MS spectra of the produced $^{13}CH_4$, ^{13}CO and $^{13}C_2H_4$ from the photocatalytic $^{13}CO_2$ reduction catalyzed by M-A(111). (d) Cycling measurements for M-A(111).

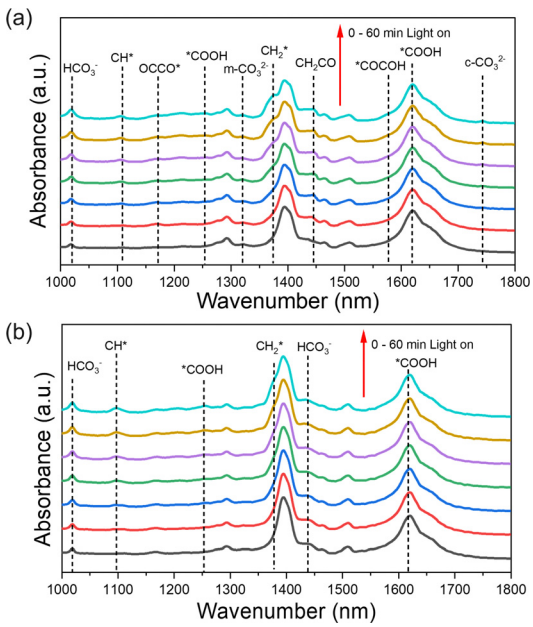

Fig. 4 *In situ* FT-IR spectra of CO_2 reduction under simulated light from 0 to 60 min for (a) M-A(111) and (b) M-A(100).

correspond to *COOH,[30,32] an important intermediate for the formation of CO and multi-carbon products. Importantly, compared to the M-A(100), M-A(111) exhibits distinctive peaks including OCCO* (1171 cm^{-1}), CH_2CO (1447 cm^{-1})[33] and *COCOH (1577 cm^{-1}),[34] which are the key intermediates for the formation of C_2H_4. This suggests that the surface of M-A(111) is more conducive to the production of C_2H_4 during the CO_2RR.

The photocatalytic reduction of CO_2 to CH_4 involves multi-steps,[35] including *CO on the MIL-101 spilling over on the PdPt alloys for weaker binding energy of CO to the MIL-101 than that to the PdPt alloys,[32,36] and *CHO, *OCH_2 and *OCH_3 formation on PdPt alloys. To better understand the *CO performance of different facets on PdPt alloys, we applied DFT calculations to investigate intermediate models in the CO_2RR process (see computing details in the ESI†). From the calculated free energy diagrams, for the PdPt(111) surface, *CO transforms to *CHO, *OCH_2 and *OCH_3 by sequential hydrogenation with energy barriers of 0.03, 0.26 and 0.19 eV for each step. In the {100} surface, the hydrogenation of CO to CH_4 is very difficult because of its high energy barriers (0.52 eV *CO to *CHO, 0.78 eV *CHO to *OCH_2) (Fig. S18, ESI†). This indicates that CH_4 formation is more favored at the {111} surface than {100} surface, which is in agreement with experiments.

In summary, this study presents an approach for designing composite photocatalysts of MOF with crystal facet engineered bimetallic alloys for the CO_2RR. A series of control experiments demonstrate that M-A(111) exhibits superior capability for the production of C_2H_4 in the photocatalytic CO_2RR. *In situ* FT-IR analysis revealed that the surface of M-A(111) more readily facilitates the formation of C_2 intermediates during the CO_2RR, resulting in a conversion rate of 9.5 μmol g^{-1} h^{-1} for C_2H_4. This work provides a new strategy for the design of photocatalysts that can enhance CO_2 photocatalytic reduction towards C_2H_4.

We gratefully acknowledge the National Natural Science Foundation of China (grant no. 22171131 and 22231006) for financial support of this work. This work was also supported by a Project Funded by the Priority Academic Program Development of Jiangsu Higher Education Institutions and the Science and Technology Department Foundation of Jiangsu Province (TC2023A001).

Data availability

The data supporting this article have been included as part of the ESI.†

Conflicts of interest

There are no conflicts to declare.

References

1 L. Wang, W. Chen, D. Zhang, Y. Du, R. Amal, S. Qiao, J. Wu and Z. Yin, *Chem. Soc. Rev.*, 2019, **48**, 5310–5349.
2 B. Zhou, Y. Ma, P. Ou, Z. Ye, X.-Y. Li, S. Vanka, T. Ma, H. Sun, P. Wang, P. Zhou, J. K. Cooper, Y. Xiao, I. A. Navid, J. Pan, J. Song and Z. Mi, *Nat. Catal.*, 2023, **6**, 987–995.
3 Y. Wu, Q. Hu, Q. Chen, X. Jiao and Y. Xie, *Acc. Chem. Res.*, 2023, **56**, 2500–2513.
4 Y. W. Choi, F. Scholten, I. Sinev and B. Roldan Cuenya, *J. Am. Chem. Soc.*, 2019, **141**, 5261–5266.
5 G. Wang, C. T. He, R. Huang, J. Mao, D. Wang and Y. Li, *J. Am. Chem. Soc.*, 2020, **142**, 19339–19345.
6 G. Wang, Z. Chen, T. Wang, D. Wang and J. Mao, *Angew. Chem., Int. Ed.*, 2022, **61**, e202210789.
7 Ş. Neaţu, J. A. Maciá-Agulló, P. Concepción and H. Garcia, *J. Am. Chem. Soc.*, 2014, **136**, 15969–15976.
8 Y. Yu, Y. He, P. Yan, S. Wang and F. Dong, *Proc. Natl. Acad. Sci. U. S. A.*, 2023, **120**, e2307320120.
9 M. Zhang, Y. Mao, X. Bao, P. Wang, Y. Liu, Z. Zheng, H. Cheng, Y. Dai, Z. Wang and B. Huang, *ACS Catal.*, 2024, **14**, 5275–5285.
10 H. Zhao, R. Yu, S. Ma, K. Xu, Y. Chen, K. Jiang, Y. Fang, C. Zhu, X. Liu, Y. Tang, L. Wu, Y. Wu, Q. Jiang, P. He, Z. Liu and L. Tan, *Nat. Catal.*, 2022, **5**, 818–831.
11 H. Lin, S. Luo, H. Zhang and J. Ye, *Joule*, 2022, **6**, 294–314.
12 F. Guo, S. Yang, Y. Liu, P. Wang, J. Huang and W. Y. Sun, *ACS Catal.*, 2019, **9**, 8464–8470.
13 X. Li, J. Yu, M. Jaroniec and X. Chen, *Chem. Rev.*, 2019, **119**, 3962–4179.
14 X. Zhang, Z. Sun, B. Wang, Y. Tang, L. Nguyen, Y. Li and F. F. Tao, *J. Am. Chem. Soc.*, 2018, **140**, 954–962.
15 R. Xu, D. H. Si, S. S. Zhao, Q. J. Wu, X. S. Wang, T. F. Liu, H. Zhao, R. Cao and Y. B. Huang, *J. Am. Chem. Soc.*, 2023, **145**, 8261–8270.
16 R. Long, Y. Li, Y. Liu, S. Chen, X. Zheng, C. Gao, C. He, N. Chen, Z. Qi, L. Song, J. Jiang, J. Zhu and Y. Xiong, *J. Am. Chem. Soc.*, 2017, **139**, 4486–4492.
17 Y. Yu, X. a Dong, P. Chen, Q. Geng, H. Wang, J. Li, Y. Zhou and F. Dong, *ACS Nano*, 2021, **15**, 14453–14464.
18 X. M. Cheng, J. Zhao and W. Y. Sun, *EnergyChem*, 2022, **4**, 100084.
19 X. M. Cheng, X. Y. Dao, S. Q. Wang, J. Zhao and W. Y. Sun, *ACS Catal.*, 2021, **11**, 650–658.
20 X. M. Cheng, P. Wang, S. Q. Wang, J. Zhao and W. Y. Sun, *ACS Appl. Mater. Interfaces*, 2022, **14**, 32350–32359.
21 Q. Liu, L. Lai, Z. Li, J. Hu, L. Zhang, W. Younas and G. Mao, *ACS Appl. Nano Mater.*, 2023, **6**, 11764–11771.
22 A. X. Yin, X. Q. Min, Y. W. Zhang and C. H. Yan, *J. Am. Chem. Soc.*, 2011, **133**, 3816–3819.
23 X. Y. Zhang, P. Wang, X. Y. Lu, Y. Zhang and W. Y. Sun, *Chem. Eng. J.*, 2023, **476**, 146560.
24 X. Y. Lu, Q. Zhou, X. Y. Zhang, Y. Zhang, F. Gong and W. Y. Sun, *J. Mater. Chem. A*, 2024, **12**, 19414–19421.
25 J. D. Xiao, L. Han, J. Luo, S. H. Yu and H. L. Jiang, *Angew. Chem., Int. Ed.*, 2018, **57**, 1103–1107.
26 P. Li, H. Hu, G. Luo, S. Zhu, L. Guo, P. Qu, Q. Shen and T. He, *ACS Appl. Mater. Interfaces*, 2020, **12**, 56039–56048.
27 X. M. Cheng, Y. Gu, X. Y. Zhang, X. Y. Dao, S. Q. Wang, J. Ma, J. Zhao and W. Y. Sun, *Appl. Catal., B*, 2021, **298**, 120524.
28 W. Yang, H. J. Wang, R. R. Liu, J. W. Wang, C. Zhang, C. Li, D. C. Zhong and T. B. Lu, *Angew. Chem., Int. Ed.*, 2021, **60**, 409–414.
29 F. Guo, R. X. Li, S. Yang, X. Y. Zhang, H. Yu, J. J. Urban and W. Y. Sun, *Angew. Chem., Int. Ed.*, 2023, **62**, e202216232.
30 L. Ren, X. Yang, X. Sun, Y. Wang, H. Li and Y. Yuan, *Angew. Chem., Int. Ed.*, 2024, **63**, e202404660.
31 B. Su, Y. Kong, S. Wang, S. Zuo, W. Lin, Y. Fang, Y. Hou, G. Zhang, H. Zhang and X. Wang, *J. Am. Chem. Soc.*, 2023, **145**, 27415–27423.
32 T. Yan, P. Wang and W. Y. Sun, *Small*, 2023, **19**, 2206070.
33 N. Y. Huang, B. Li, D. Wu, Z. Y. Chen, B. Shao, D. Chen, Y. T. Zheng, W. Wang, C. Yang, M. Gu, L. Li and Q. Xu, *Angew. Chem., Int. Ed.*, 2024, **63**, e202319177.
34 H. Shi, Y. Liang, J. Hou, H. Wang, Z. Jia, J. Wu, F. Song, H. Yang and X. Guo, *Angew. Chem., Int. Ed.*, 2024, **63**, e202404884.
35 X. Nie, X. Jiang, H. Wang, W. Luo, M. J. Janik, Y. Chen, X. Guo and C. Song, *ACS Catal.*, 2018, **8**, 4873–4892.
36 F. Li, Y. C. Li, Z. Wang, J. Li, D. Nam, Y. Lum, M. Luo, X. Wang, A. Ozden, S. F. Hung, B. Chen, Y. Wang, J. Wicks, Y. Xu, Y. Li, C. M. Gabardo, C. T. Dinh, Y. Wang, T. T. Zhuang, D. Sinton and E. H. Sargent, *Nat. Catal.*, 2020, **3**, 75–82.

